Energy Advances

ROYAL SOCIETY OF CHEMISTRY

PAPER

View Article Online
View Journal | View Issue

Open Access Article. Published on 18 April 2023. Downloaded on 12/4/2025 3:24:02 PM.
This article is licensed under a Creative Commons Attribution 3.0 Unported Licence.

Check for updates

Cite this: *Energy Adv.*, 2023, 2, 829

Copper and iron co-doping effects on the structure, optical energy band gap, and catalytic behaviour of Co_3O_4 nanocrystals towards low-temperature total oxidation of toluene†

Hippolyte Todou Assaouka,[a] Issah Ngouh Nsangou,[a] Daniel Manhouli Daawe,[b] Daniel Onana Mevoa,[a] Abraham Atour Zigla,[b] Patrick Ndouka Ndouka[a] and Patrick Mountapmbeme Kouotou *[bcd]

This study reports the effect of Cu and Fe addition on the structure, morphology, optical energy band gap and the catalytic performance of Co_3O_4 nanocrystals (NCs). Single-oxide (CuO, Fe_3O_4, and Co_3O_4) and trimetallic oxide ($Cu_{0.75}Fe_{0.25}Co_2O_4$) NCs were prepared by a co-precipitation technique. The physico-chemical properties of the as-prepared NCs were thoroughly investigated and their performance as catalysts was successfully evaluated. Compared with single oxides, the $Cu_{0.75}Fe_{0.25}Co_2O_4$ spinel with a dome top-like morphology exhibited the highest performance with almost 100% oxidation of C_7H_8 at 220 °C at a gas hourly space velocity (GHSV) of 22 500 mL g^{-1} h^{-1}. The sequence of the catalytic performance was found to be proportional to the activation energy (E_a (kJ mol^{-1})) and the performance order is as follows: $Cu_{0.75}Fe_{0.25}Co_2O_4$ (35.2) > Co_3O_4 (55.5) ∼ CuO (75.5) > Fe_3O_4 (83.4). The excellent performance of $Cu_{0.75}Fe_{0.25}Co_2O_4$ towards toluene total oxidation is suggested to be assigned to the Cu and Fe co-doping effect and behave as promoters in the matrix of the Co_3O_4 spinel. The promotion effect can be ascribed to: (a) the smallest crystallite grain size as responsible for the largest surface specific area, (b) the lowest-temperature reducibility responsible for the highest population of oxygen vacancies, (c) the highest mobility of oxygen species due to its good redox capability and (d) the highest ratio of active species (O_{Lat}/O_{Ads}, Co^{3+}/Co^{2+}, Cu^{2+}/Cu^{+}, and Fe^{3+}/Fe^{2+}) and the lowest E_g^{opt}. The overall findings suggest that toluene total oxidation over $Cu_{0.75}Fe_{0.25}Co_2O_4$ might follow a Mars van Krevelen process.

Received 20th February 2023,
Accepted 17th April 2023

DOI: 10.1039/d3ya00082f

rsc.li/energy-advances

1. Introduction

Volatile organic compounds (VOCs) released by factories, transportation as well as human activities are well known as hazardous air waste due to their toxic, mutagenic and cyanogenic nature. VOCs are also great precursors of ozone and smog in the atmosphere.[1–3] Low-temperature catalytic oxidation is established as an effective approach for mitigating environmental emission, owing to its inexpensive operating cost, low energy consumption, high conversion efficiency and low thermal NOx emissions.[4,5] Presently, two types of catalysts, namely, supported noble metals (Ag, Au, Pt and Pd)[6–9] and metal oxides are established for the total conversion of toluene.[10–15] Particularly, transition metal oxides (TMOs) possess the advantages of availability, low cost, high thermal stability, considerable reducibility, strong resistance to poisons and promising catalytic performance.[16–18] Therefore, TMOs have attracted much attention in the total abatement of VOCs. Recently, TMO catalysts have drawn considerable attention owing to their synergistic effect with numerous advantageous properties.[19] Referring to single-metal oxides, Co_3O_4 has gained growing interest as an effective, inexpensive and active catalyst with comparable performance to supported precious metal catalysts.

Earlier, numerous synthesis approaches have been applied to fabricate Co_3O_4 in the form of thin films or powder nanocrystals (NCs) with various morphologies and physico-chemical

[a] Department of Chemistry, Faculty of Sciences, University of Maroua, Maroua P.O. Box 55, Cameroon
[b] National Advanced School of Engineering, University of Maroua, P.O. Box. 46, Maroua, Cameroon
[c] Advanced School of Agriculture, Forestry, Water and Environment, University of Ebolowa, P.O. Box 786, Ebolowa, Cameroon
[d] Institute of Engineering Thermophysics, Chinese Academy of Sciences, Beijing 100190, China. E-mail: mkpatrick1982@gmail.com

† Electronic supplementary information (ESI) available: ESI 1: catalyst characterization technique(s); ESI 2: catalytic performance measurement conditions; ESI 3: FTIR analysis details; Fig. S1: FTIR spectra of single oxide; Fig. S2: FTIR spectrum of ternary oxide; Fig. S3: EDS spectra of singles oxides; Fig. S4: Auger spectrum; Table S1: H_2-TPR quantitative data. See DOI: https://doi.org/10.1039/d3ya00082f

© 2023 The Author(s). Published by the Royal Society of Chemistry

Open Access Article. Published on 18 April 2023. Downloaded on 12/4/2025 3:24:02 PM.
This article is licensed under a Creative Commons Attribution 3.0 Unported Licence.

properties. However, the good activity of Co_3O_4 towards the total conversion of VOCs was assigned more to the high specific surface area and the occurrence of oxygen vacancies than to the ordered structures.[6] Analogously, acidic leaching has been used as a strategy to modify the chemistry and structure of Co_3O_4, and the as-synthesized Co_3O_4 NCs with mesoporous structure exhibit improved performance towards toluene conversion into CO_2 and H_2O.[10] The better surface specific area, abundant surface Co^{2+}, adsorbed oxygen ($O_{Ads.}$) species and/or oxygen vacancy (O_v) were reported to play a decisive role in the catalytic oxidation process.[20,21] Despite the previously applied strategy, there is significant interest in enhancing the catalytic performance of Co_3O_4 for various VOCs in order to expand the range of feasibility and meet the requirements of practical applications in catalysis. Therefore, a doping strategy which consists of the substitution and/or addition of a second metal cation in the Co_3O_4 lattice is presently investigated as a prospective route to additionally improve the performance of Co_3O_4 catalysts.

Recently, extensive practical and theoretical investigation on the influence of transition metal cation dopant features on the physicochemical and redox properties of cobalt-based binary oxide catalysts have been reported.[10,14] The authors have established that doping could redesign the chemical composition and ionic states, ionic radius, as well as chemical bonding in the bulk and surface of Co_3O_4, which might result in an excellent catalytic performance.

To date, several binary metal (Mn, Cu, Ni, and Fe)-doped Co_3O_4 thin films and nanocrystal powder have been prepared and successfully tested as catalysts.[13,15,22] Among TMO-based catalysts, Co–Cu and Co–Fe oxide catalysts exhibit promising performance in the elimination of VOCs. In fact, by introducing different types of transition metals (TMs) into the pure TMO lattice, the redox behaviour and chemical activity of the obtained mixed-TMO can be modified due to many factors.[23,24] On the structural aspect, numerous defects with high chemical activity can be formed due to the stress provoked by doping or insertion of a second metal in the matrix of a single TMOs. In addition, TM ↔ TM or TM ↔ oxygen ↔ TM can open the way to new electronic properties, absent in single TMOs.[25]

Although doping has a significant impact on the catalytic behavior of individual oxides, research has mainly focused on binary oxides, and there have been only a few studies investigating catalytic oxidation with ternary or trimetallic oxide-based TMs.[13,26] However, it is not *a priori* clear what type and number of metals are required to enhance single-TMO catalytic activity and the lattice stability at high temperatures. Ternary oxides are generally used as electrocatalysts with a wide variety of critical physicochemical properties and excellent stability for several applications; such materials can also be highly active catalysts and display an exceptional activity compared to single and binary oxides.[27,28] Recently, Waqas *et al.*, have reported a preliminary study on the application of Cu–Co–Fe oxide thin films as catalysts for low-temperature CO, although it has shown a potential catalytic application, the as-prepared catalyst shows weak stability and durability upon continuous time-on-stream.[29] It is therefore interesting to perform a systematic study on the influence of both Cu and Fe with appropriate contents on the properties of Co-based oxides. The designed ternary oxide CuFeCoO is expected to exhibit superior properties beneficial for the catalytic performance and stability.

Herein, three single-oxide (CuO, Co_3O_4, and Fe_3O_4) and one trimetallic oxide ($Cu_{0.75}Fe_{0.25}Co_2O_4$) catalysts were prepared by a co-precipitation technique. The as-prepared catalysts were thermally treated before their use as catalysts for toluene oxidation. Particularly, attention was paid to understand the influence of Cu and Fe co-doping on the physicochemical and catalytic properties of the as-prepared NCs. An attempt was made to correlate the catalytic behavior of $Cu_{0.75}Fe_{0.25}Co_2O_4$ NCs with the abundant metallic surface and reactive oxygen species, and open porosity of NCs with high S_{BET}, as well as the highest reducibility and lowest E_g^{opt}.

2. Results and discussion

2.1. Structure and texture of catalysts by XRD

The structures of CuO, Fe_3O_4, Co_3O_4 and $Cu_{0.75}Fe_{0.25}Co_2O_4$ were examined by XRD, as displayed in Fig. 1, while the summary quantification details are shown in Table 1. The XRD spectrum of Fe_3O_4 exhibited a peak located at 2θ = 30.8°, 35.75°, 43.92°, 58.52° and 64,20°, which could be assigned to the (220), (311), (400), (440), and (622) crystal planes (JCPDS No. 01-075-0449) respectively. For the Co_3O_4 sample, the crystal structure and diffraction signals at 2θ values of 31.5°, 35.81°, 36.78°, 43.95°, 58.33° and 64.18° could be assigned to the (220), (311), (222), (400), (440), and (533) crystal planes (JCPDS No. 74-1656) respectively. As for CuO, two prominent peaks located at 35.3° (002) and 38.6° (111) are detected on the diffraction spectrum, which can be perfectly indexed to monoclinic CuO

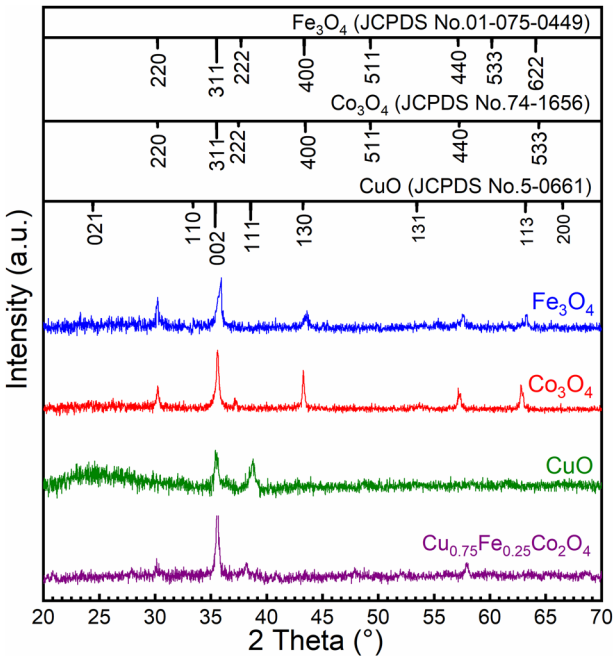

Fig. 1 XRD patterns of CuO, Fe_3O_4, Co_3O_4 and $Cu_{0.75}Fe_{0.25}Co_2O_4$ NPs.

 © 2023 The Author(s). Published by the Royal Society of Chemistry

Open Access Article. Published on 18 April 2023. Downloaded on 12/4/2025 3:24:02 PM.
This article is licensed under a Creative Commons Attribution 3.0 Unported Licence.

Table 1 Summary catalysts characteristic including: particle size, specific surface area, TPR peaks, activation energy and temperature at 90% conversion of toluene

Samples	PS[a] (nm)	S_{BET}[b] ($m^2\ g^{-1}$)	T (°C) TPR[c] peaks	E_a[d] (kJ mol^{-1})	T_{90}[e] (°C)
Co_3O_4	60	48	390[x] and 487[y]	75.5	250
CuO	14	87	251[x]	55.5	250
Fe_3O_4	50	23	438[x] and 720[y]	83.4	270
$Cu_{0.75}Fe_{0.25}Co_2O_4$	18	137	180[x], 210[y] and 249[z]	35.2	225

[a] Average crystallite size. [b] Specific surface area by BET method. [c] H_2-temperature programmed reduction ([x]1st, [y]2nd k and [z]3rd peak). [d] Activation energy. [e] Temperature at 90% conversion.

(JCPDS no. 05-0661). No other characteristic diffraction peaks including CoO, Co_2O_3, and FeO were detected in these single oxides, attesting for the purity of samples. However, $Cu_{0.75}Fe_{0.25}Co_2O_4$ samples with a spinel exhibit clear signals, which fit well with some XRD diffraction peaks characteristic of Co_3O_4, Fe_3O_4 and CuO single oxides. The obtained XDR spectrum is in close agreement with early reported results.[30] Additionally, no other specific signals were observed, which attest of the purity of the as-prepared samples. The particle sizes of all the samples were estimated from the most intense diffraction signals using Scherrer's formula. The crystallite size was calculated to be 18 ± 2 nm, as displayed in Fig. 1. The crystallite size of the $Cu_{0.75}Fe_{0.25}Co_2O_4$ sample was found to be smaller than the ones of CuO (~14 nm), Fe_3O_4 (~50 nm) and Co_3O_4 (~60 nm) respectively, suggesting that $Cu_{0.75}Fe_{0.25}Co_2O_4$ facilitates high dispersion.[31] Furthermore, it is well established that a small particle size showed a beneficial effect on the active site dispersion.[32] The synergy between Fe, Cu, and Co species and the $Cu_{0.75}Fe_{0.25}Co_2O_4$ structure is expected to play an important role in the C_7H_8 total oxidation process that could improve the catalytic performance.

2.2. Fourier transform infra-red analysis

FTIR emission was also performed in order to analyze the functional group at the surface of CuO, Co_3O_4, Fe_3O_4 and $Cu_{0.75}Fe_{0.25}Co_2O_4$ samples. The FTIR spectrum of singles and trimetallic oxides and their corresponding description are presented in ESI 3† (Fig. S1 and S2 respectively).

2.3. Morphology analysis

The microstructural features of $Cu_{0.75}Fe_{0.25}Co_2O_4$, CuO, Co_3O_4, and Fe_3O_4 samples were studied using a scanning electron microscope, as displayed in Fig. 2. Fe_3O_4 catalysts present a needle-like morphology (Fig. 2a and b), resulting from the aggregation of narrow particles to form clusters with an average crystallite size of ~50 nm.[33] From Fig. 2c and d, it was observed that the Co_3O_4 sample exhibits a cubic-like morphology formed by quasi uniform microstructures with a grain size of different diameters and the average diameter estimated to be approximately ~60 nm. Fig. 2e and f present the CuO micrograph images, with regular and uniform particles strongly agglomerated together and which form regular grains of same shape and size (~14 nm). Fig. 2g and h show $Cu_{0.75}Fe_{0.25}Co_2O_4$, with dome top-like morphology composed of small particles (~18 nm). Moreover, the dome top-like morphology of

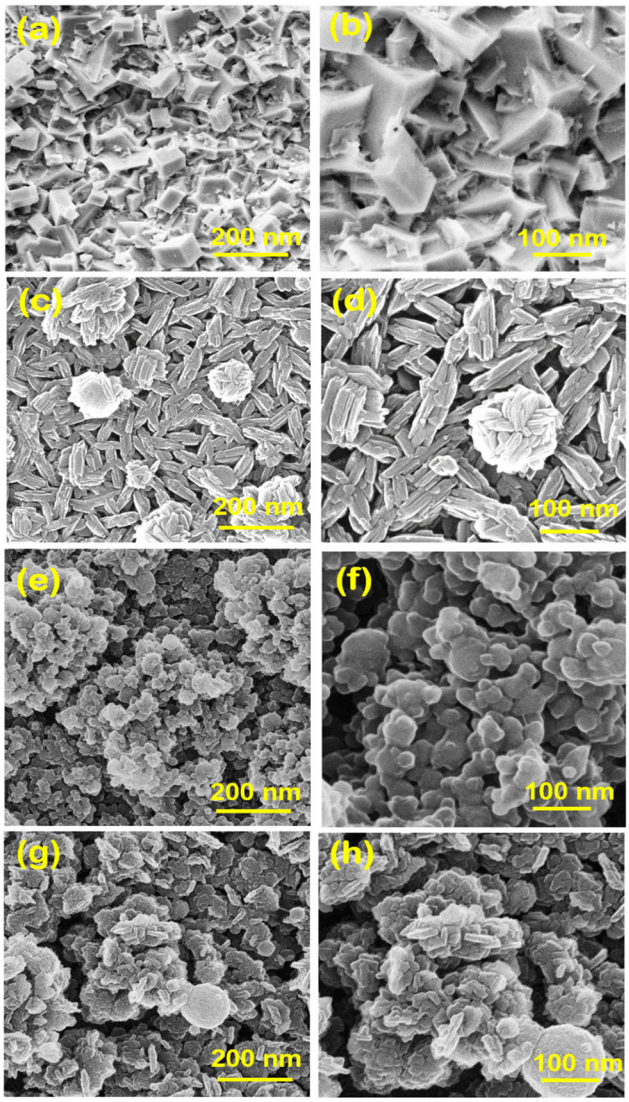

Fig. 2 Low- and high-magnification SEM images of spinel Co_3O_4 (a and b), Fe_3O_4 (c and d), CuO (e and f), and $Cu_{0.75}Fe_{0.25}Co_2O_4$ (g and h).

$Cu_{0.75}Fe_{0.25}Co_2O_4$ increases the specific surface area (137 $m^2\ g^{-1}$) of the targeted catalyst, which additionally furnishes further sites for electrophilic species (O_2^{2-} or O^-) accumulation, minimizing the diffusion length of oxygen species.[34] Aside from the dome top-like structure, considerable narrow holes (open porosity) are also detected and are suggested to be created due

Open Access Article. Published on 18 April 2023. Downloaded on 12/4/2025 3:24:02 PM.
This article is licensed under a Creative Commons Attribution 3.0 Unported Licence.

to competitive growth among Cu, Fe and Co oxides during the co-precipitation. Therefore, these small holes, surface open porosity, and increased surface area of the catalysts potentially consisted of more chemisorbed and physisorbed surface-active oxygen species are expected to play an important role in catalytic performance in agreement with the literature.[35]

2.4. Bulk composition (EDS)

Energy-dispersive spectroscopy (EDS) was employed to analyze the bulk composition of the overall catalysts. Since our main target in this study is the trimetallic oxide, we present the corresponding EDS spectrum of $Cu_{0.75}Fe_{0.25}Co_2O_4$ (Fig. 3) in the main manuscript, and spectra for Co_3O_4, CuO and Fe_3O_4 can be found in the ESI† (Fig. S3). As presented in Fig. 3, the EDS result of the obtained ternary $Cu_{0.75}Fe_{0.25}Co_2O_4$ displays peaks corresponding to iron (Fe: 6.20%), copper (Cu: 8.00%), carbon (C: 1.36%), cobalt (Co: 21.7%), and oxygen (O: 49.24%) elements. The EDS results for single metal oxides revealed the atomic percentages of elements as follows: CuO: 50.76% Cu and 50.24% O; Co_3O_4: 53.18% Co and 46.82% O; and Fe_3O_4: 48.72 Fe and 51.28% O free of all other metals and contaminants. These findings confirm on the chemically pure nature of the synthesized oxides by a precipitation method.

2.5. Composition and ionic states (XPS)

The surface chemical composition and ionic states of CuO, Co_3O_4, Fe_2O_3 and $Cu_{0.75}Fe_{0.25}Co_2O_4$ were analyzed by XPS, as shown in Fig. 4, and the related characteristic details are listed in Table 2. The Fe 2p spectra of $Cu_{0.75}Fe_{0.25}Co_2O_4$ and Fe_2O_3 exhibit a significant peak at 711.15 and 780.7 eV, assigned to the Fe $2p_{3/2}$ and Fe $2p_{1/2}$ core shell respectively, in close agreement with the reported value.[36] The Fe $2p_{3/2}$ spectra of $Cu_{0.75}Fe_{0.25}Co_2O_4$ are separated into Fe^{3+} and Fe^{2+} components at 779. 7 and ~781 eV respectively, while and Fe $2p_{1/2}$ is also deconvoluted into the same constituents located at 725.8 and 727.45 eV, respectively. The signals at ~718 and ~734 eV correspond to satellite peaks. The deconvolution results of the Fe_3O_4 spectrum showed two components at 727.03 and 728.10 eV, which could be attributed to the Fe^{2+} and Fe^{3+} species, respectively. This attribution is based on the close value (8.47 eV) of the spin-orbital splitting reported earlier in the literature.[37] Additionally, satellite peaks are observed at lower (~731.15 eV) and higher (~739.62 eV) binding energies. Similarly, the Co 2p XPS profile for $Cu_{0.75}Fe_{0.25}Co_2O_4$ and Co_3O_4 exhibited two significant peak located at 780.6 and 796.7 eV respectively assigned to Co $2p_{3/2}$ and Co $2p_{1/2}$, in close agreement with the literature.[38,39]

The Gaussian fitting data show two signals that could be deconvoluted into two doublets, suggesting the coexistence of Co cations in both divalent- (Co^{2+}) and trivalent (Co^{3+}) oxidation states at the surface as well as in the lattice of $Cu_{0.75}Fe_{0.25}Co_2O_4$. The signals located at ~780.01 and ~796.7 eV were associated with the presence of Co^{3+}, whereas the peaks centered at ~781.1 and ~795.9 eV were allied to the occurrence of Co^{2+} species in $Cu_{0.75}Fe_{0.25}Co_2O_4$.[39,40] It is worth that, the signals at ~790.02 eV were assigned to satellite signals. Following the same procedure, Co_3O_4 fitting results displayed the Co 2p spectrum with asymmetric peaks, with an evident shift of BE towards to higher values and which is made of several overlapping features emerging from $2p_{3/2}$ (~783.3 eV) and $2p_{1/2}$ (~796.5 eV) signals ascribed to Co^{2+} and Co^{3+}. Satellite peaks were detected at low BE (~788.5 eV).[41] Finally, $Cu_{0.75}Fe_{0.25}Co_2O_4$ and CuO exhibit two intense signals centered at ~952.0 and ~931.9 eV assigned to Cu $2p_{1/2}$ and Cu $2p_{3/2}$, respectively.[42] Since the discrimination of different Cu oxidation states (Cu^0 Cu^+ and Cu^{2+}) by XPS cannot be easily

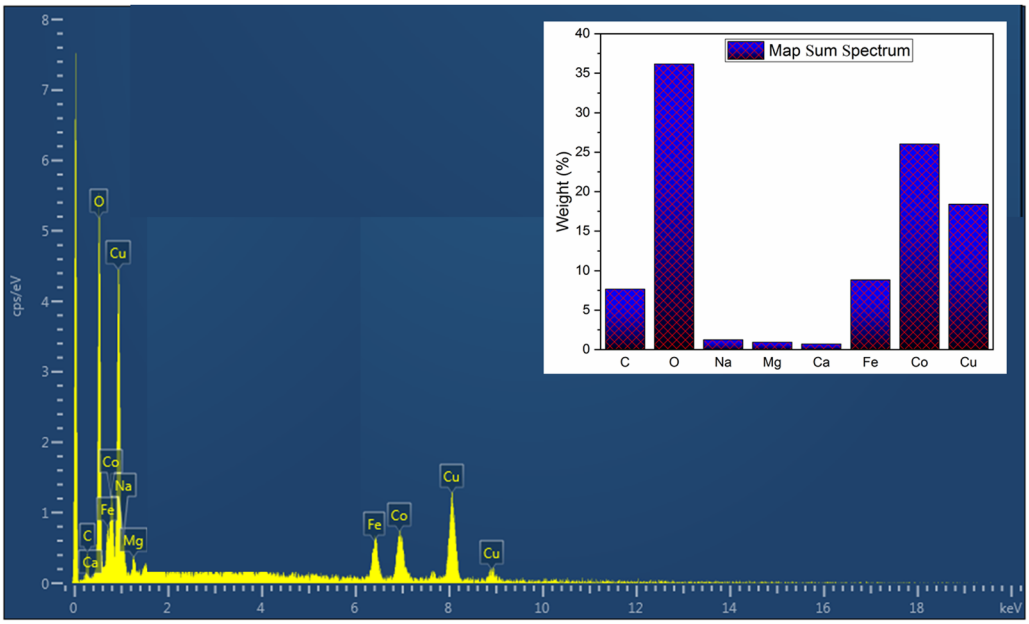

Fig. 3 EDS spectrum of $Cu_{0.75}Fe_{0.25}Co_2O_4$ nanoparticles.

 © 2023 The Author(s). Published by the Royal Society of Chemistry

Open Access Article. Published on 18 April 2023. Downloaded on 12/4/2025 3:24:02 PM.
This article is licensed under a Creative Commons Attribution 3.0 Unported Licence.

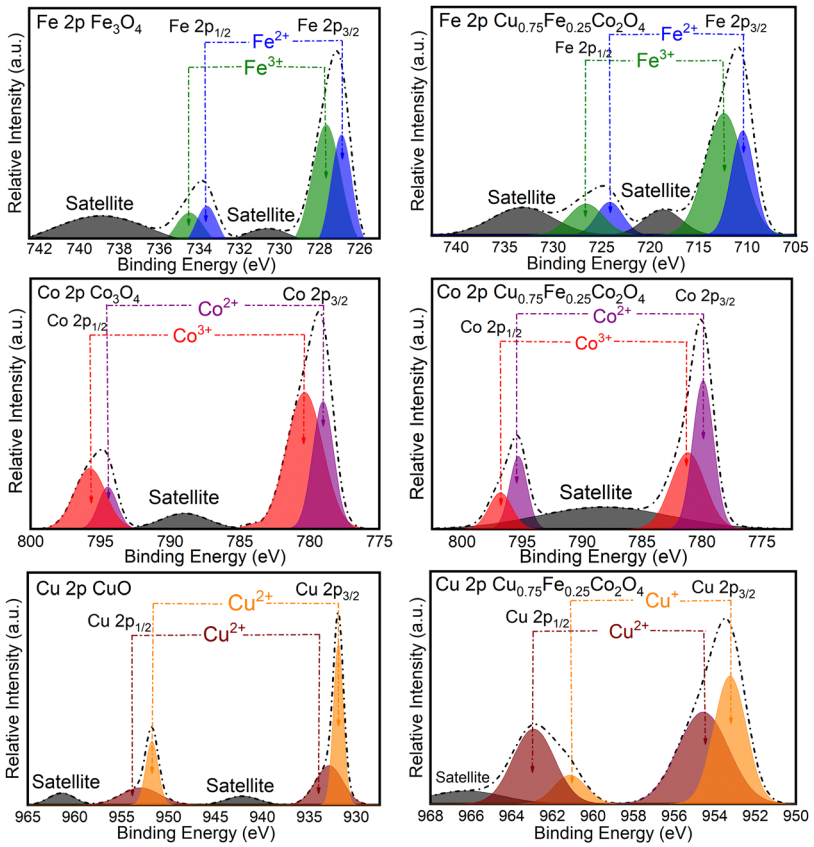

Fig. 4 XPS spectra of Co 2p, Fe 2p, and Cu 2p of CuO, Co_3O_4, Fe_3O_4 and $Cu_{0.75}Fe_{0.25}Co_2O_4$.

Table 2 Summary of XPS peaks-fitting results: O1s binding energies, relative atomic percentage and corresponding ratios of $O_{Ads.}$ and O_{Lat} for CuO, Co_3O_4, Fe_3O_4, and $Cu_{0.75}Fe_{0.25}Co_2O_4$

				$O_{Lat.}$ (CuO/CoO/FeO/CuCoFeO)		$O_{Ads.}$ (–OH)		$O_{Ads.}$ ($-CO_3^{2-}$)			
Samples	Co^{3+}/Co^{2+} (%)	Fe^{3+}/Fe^{2+} (%)	Cu^{2+}/Cu^{+} (%)	At (%)	BE (eV)	At (%)	BE (eV)	At (%)	BE (eV)	$O_{Ads.}/O_{Lat.}$ (%)	O_v (%)
CuO	—	—	0.48	48.58	529.50	17.42	531.80	03.74	532.90	0.45	49.36
Co_3O_4	0.43	—	—	50.94	529.10	25.30	530.14	50.62	532.26	0.55	56.34
Fe_3O_4	—	0.46	—	58.16	529.85	20.93	530.42	—	—	0.36	41.18
$Cu_{0.75}Fe_{0.25}Co_2O_4$	0.57	0.54	0.52	33.12	53.50	63.23	532.15	—	—	1.90	71.25

Note: BE stands for binding energy; At% is the atomic percentage.

performed, the Auger spectrum was recorded, and is shown in Fig. S4 (ESI†). As displayed in Fig. S4 (ESI†), a comparison with the characteristic feature of Cu LMM BE located at ~934.1 eV for CuO samples (in Fig. S4a, ESI†) indicates that Cu^0 and Cu^+ do not seem to be present in the as-prepared CuO NPs. Moreover, the signals at ~953.05 and ~963.07 eV with the difference of ~10.02 eV showed that copper in $Cu_{0.75}Fe_{0.25}Co_2O_4$ exhibits mainly II+ oxidation state.[11] Therefore, one can conclude that the oxidation state of copper in CuO NPs is mainly Cu^{2+}, in excellent agreement with the literature.[43,44] In contrast, the characteristic feature of Cu LMM for $Cu_{0.75}Fe_{0.25}Co_2O_4$ NPs (see Fig. S4b, ESI†) is located at ~954.7 eV. By comparison with the chemical shifts of the standard sample, the bands located at a binding energy ranging from 961.00 to 948.00 eV could be ascribed to the states of both Cu^{2+} and Cu^+, in good agreement with the literature.[45]

The O 1s core–shell spectra of the synthesized oxides have been recorded and deconvoluted into several prominent peaks, as shown in Fig. 5. The O 1s patterns of the $Cu_{0.75}Fe_{0.25}Co_2O_4$ sample exhibit a close profile to that of CuO and a totally different profile to that of Fe_3O_4 and Co_3O_4. From the XPS spectra profiles, two to three prominent signals located at BEs of ~529, ~531 and ~532 eV were detected. The most prominent signal detected at the lowest BE (~529.5 eV) could be ascribed to the lattice oxygen ($O_{Lat.}$) in the metal ($Cu_{0.75}Fe_{0.25}Co_2O_4$, CuO, Fe_3O_4 and Co_3O_4)–oxygen framework or electrophilic oxygen species (O_2^-) in surface oxygen vacancies (O_v) and adsorbed oxygen ($O_{Ads.}$), respectively. The two

Open Access Article. Published on 18 April 2023. Downloaded on 12/4/2025 3:24:02 PM.
This article is licensed under a Creative Commons Attribution 3.0 Unported Licence.

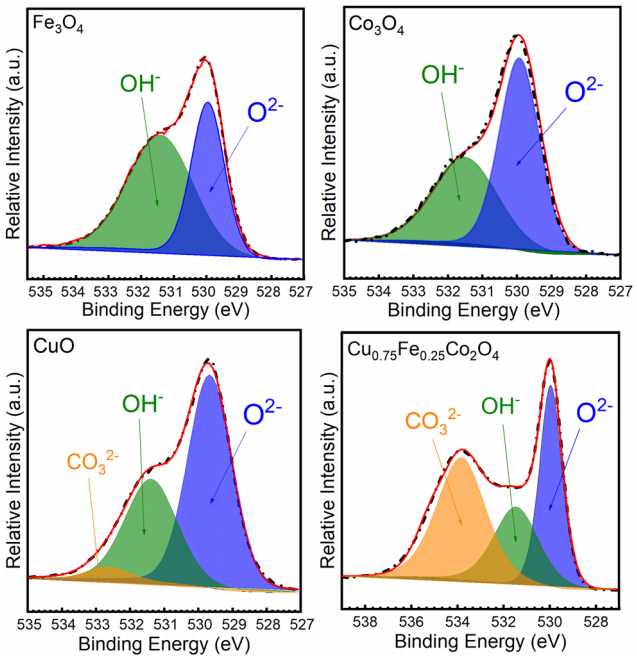

Fig. 5 XPS spectra of O 1s of CuO, Co_3O_4, Fe_3O_4 and $Cu_{0.75}Fe_{0.25}Co_2O_4$.

other signals detected at ~531.2 and ~532.3 eV were ascribed to the hydroxyl (OH^-) and carbonyl groups weakly bonded at the surface of the metal oxide, respectively.[46] As for $Cu_{0.75}Fe_{0.25}Co_2O_4$, for which the peaks of $O_{Ads.}$ were most intense than that of $O_{Lat.}$, a completely different profile was shown. The proportions of surface oxygenated species and their ratio ($O_{Lat.}/O_{Ads.}$) were estimated, and the results are summarized in Table 2. The highest $O_{Ads.}/O_{Lat.}$ ratio of ~1.90 was obtained for the $Cu_{0.75}Fe_{0.25}Co_2O_4$ catalyst, while those of Co_3O_4 (~0.55), CuO (~0.45) and Fe_3O_4 (~0.36) were remarkably lower. Obviously, $Cu_{0.75}Fe_{0.25}Co_2O_4$ exhibits the largest content of O_{Ads}. It is well known that the $O_{Ads.}/O_{Lat.}$ ratio on the metal oxide catalyst surface attests to the presence of more active Ov species.[47] $O_{Ads.}$ and $O_{Lat.}$ are reported to be strongly reactive sites that can attack VOCs in the neighborhood of the maximum electron density and thereby oxidize the carbon framework.[48] The presence of superabundant oxygen species and O_2^{2-} or O^- is well known to be beneficial for the catalytic oxidation of CO and C_7H_8.[49] In this regard, it will be rational to deduce that the C_7H_8 catalytic oxidation process over $Cu_{0.75}Fe_{0.25}Co_2O_4$ can occur on $O_{Ads.}$ and/or on $O_{Lat.}$in the present investigation.

2.6. Optical energy band gap analysis

Further characterization of the single (CuO, Fe_3O_4, and Co_3O_4) and ternary ($Cu_{0.75}Fe_{0.25}Co_2O_4$) oxides was achieved by UV-Vis absorption spectroscopy, and typical spectra are shown in Fig. 6. In Fig. 6a, c, e and g, the characteristic bands of each sample were observed, with the absorption spectra decreasing as the wavelength increased in the visible region. These observations are in good agreement with the literature.[50] The obtained absorption spectra were used to estimate the bandgap energies from Tauc's equation, and corresponding Tauc plot obtained from $(\alpha h\upsilon)^2$ *vs.* $h\upsilon$ is presented in Fig. 6b, d, f and h. The targeted sample $Cu_{0.75}Fe_{0.25}Co_2O_4$ exhibits two optical energy bandgap (E_g^{Opt}) at 1.2 and 1.55 ± 0.05 eV, values that are much smaller than that of CuO (~2.65 eV), Fe_3O_4 (~2.75 eV), and Co_3O_4 (~1.85 and 3.4 eV), respectively. The occurrence of three transition metals with different oxidation states may have provoked microstructural modification as well as an interruption of the band structure, causing the shift of $Cu_{0.75}Fe_{0.25}Co_2O_4$ E_g^{Opt} towards a lower value. Additionally, it is well established that the particle size of metals in addition oxides can be used to monitor E_g^{Opt}, and metal oxides catalysts with small particles size generally exhibits narrow E_g^{Opt}.[51] From a physical point of view, two fundamental reasons in relation to the presence of oxygen vacancies (O_v) and several metals in the matrix of mixed oxides can explain the decrease in E_g^{Opt} of mixed metal oxide. Firstly, doping can induce an increase of the O_v population in both surface and bulk of the mixed oxides, which, in turn, promotes delocalization of the defect states near the valence band edge. This leads to a decrease in E_g^{Opt} due to the overlap with the valence band edge, causing the top of the valence band to shift to the forbidden gap.[52] Second, metal excess (nonstoichiometric O_v) or deficiency (oxygen excess) in the matrix of mixed oxide induces n-type conductivity and p-type conductivity respectively.[53] Therefore, as the O_v concentration gradually increases upon doping, a considerable increase in the electron mass in the conduction band occurs, forcing edge band conduction into the bandgap that, in turn, becomes narrower.[54] It is therefore suggested that the observed reduction in the bandgap of $Cu_{0.75}Fe_{0.25}Co_2O_4$ nanocrystals can be correlated with O_v created due to the Cu and Fe co-doping,[55] as well as with the narrowest particle size displayed by the ternary oxide, as evidenced by XPS, XRD, and SEM analyses. Kouotou *et al.*[11] have previously reported a close correlation between E_g^{Opt} and the metal oxide catalytic behavior in the oxidation processes. The lowest E_g^{Opt} obtained for $Cu_{0.75}Fe_{0.25}Co_2O_4$ in the present work could facilitate electron mobility in the matrix of the trimetallic oxide and thus enhanced its catalytic performance.[56]

2.7. Temperature-programmed reduction under H_2 flow analysis (H_2-TPR)

Temperature-programmed reduction under H_2 flow (H_2-TPR) is a well-established and suitable approach to study the reducibility potential of catalysts. In this work, H_2-TPR was performed at a temperature ranging from 100 to 700 °C, as depicted in Fig. 7. The Fe_3O_4 spectrum shows two reduction peaks, at ~330 and ~580 °C, which were ascribed to the reduction of Fe^{3+} to Fe^{2+} and of Fe^{2+} to Fe^0 respectively. The characteristic peaks of Co_3O_4 sample located at ~290 and ~385 °C were assigned to the reduction of Co^{3+} to Co^{2+} and Co^{2+} to Co^0, respectively.[10,19] As far as the H_2-TPR profile of CuO is concerned, a single reduction peak at ~254 °C was observed, which could be attributed to the reduction of Cu^{2+} to Cu^0. Furthermore, three distinct and prominent reduction peaks at 180, 210 and ~249 °C, which could be ascribed to Cu^{2+} to Cu^0, Co^{3+} to Co^0 and Fe^{3+} to Fe^0 respectively were identified for the

 © 2023 The Author(s). Published by the Royal Society of Chemistry

Open Access Article. Published on 18 April 2023. Downloaded on 12/4/2025 3:24:02 PM.
This article is licensed under a Creative Commons Attribution 3.0 Unported Licence.

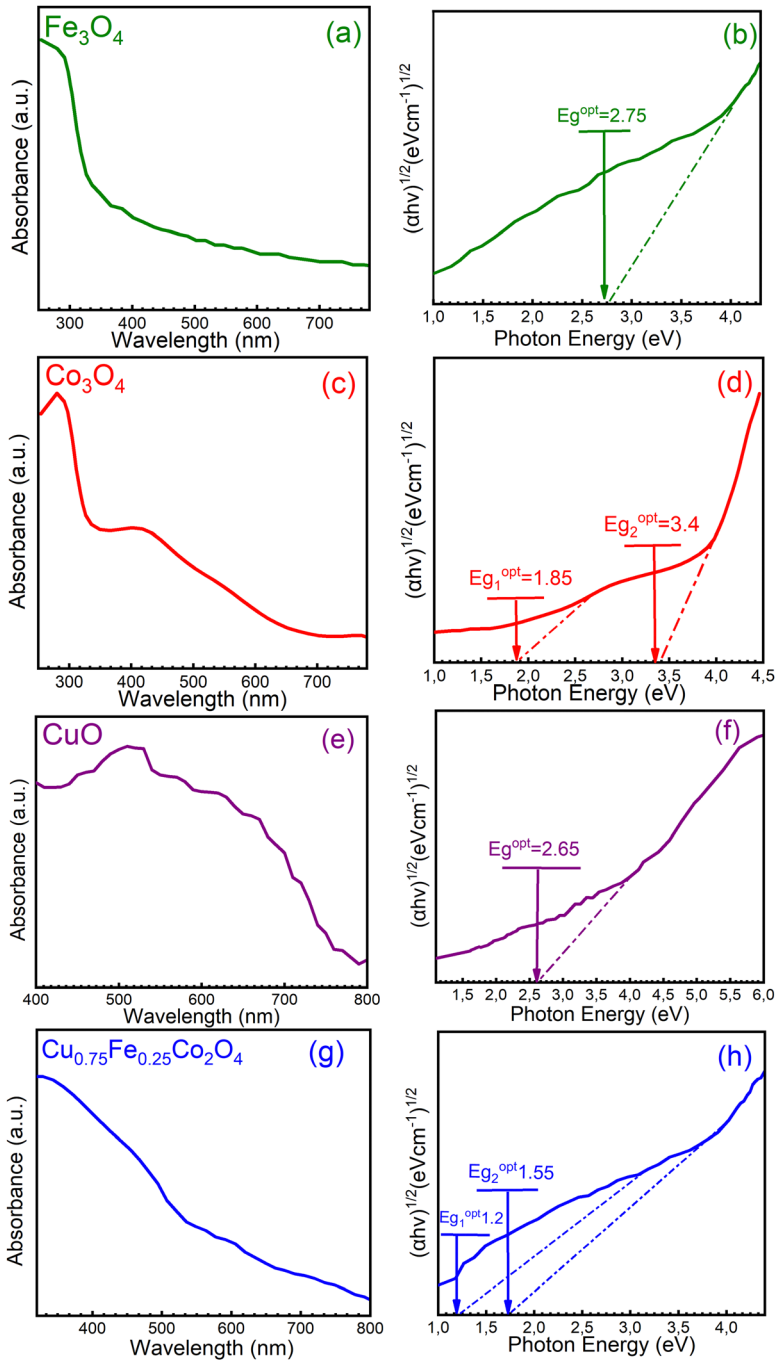

Fig. 6 UV-Vis spectrum (a, c, e and g) and (b, d, f and h) $(ah\nu)^2$ *vs.* $h\nu$ for (a and b) Fe_3O_4, (c and d) Co_3O_4, (e and f) CuO, and (g and h) $Cu_{0.75}Fe_{0.25}Co_2O_4$.

$Cu_{0.75}Fe_{0.25}Co_2O_4$ spinel, which is in good agreement with previous reported studies.[57] According to the detailed quantitative results from Table 3, the relative peak area ratio of peak I and peak II was equal to ~3.15 for the Co_3O_4 catalyst, which was slightly superior to the theoretical ratio of 3, which probably revealed an incomplete reduction of Co^{3+} to Co^{2+} during the first reduction peak. Compared to pure Co_3O_4, the reduction processes over $Cu_{0.75}Fe_{0.25}Co_2O_4$ shifted to much lower temperatures, with the first peak moving to 180 °C and the second peak to 249 °C. The left-shift of the reduction temperature was a typical signal for better reducibility. In addition, the relative area ratio between peak I and peak II decreased to 1.70, which was lower than the theoretical value of Co_3O_4 and could be due to the co-doping of Co_3O_4 with both Cu and Fe, which have generated more active surface oxygen species (see XPS results) over $Cu_{0.75}Fe_{0.25}Co_2O_4$, which coupled with H_2 at a relatively low-temperature. We can therefore conclude that the synergistic interaction between dopants (Cu and Fe) and Co_3O_4 caused facile and complete reduction of $Cu_{0.75}Fe_{0.25}Co_2O_4$ at lower temperatures, which have easily

Open Access Article. Published on 18 April 2023. Downloaded on 12/4/2025 3:24:02 PM.
This article is licensed under a Creative Commons Attribution 3.0 Unported Licence.

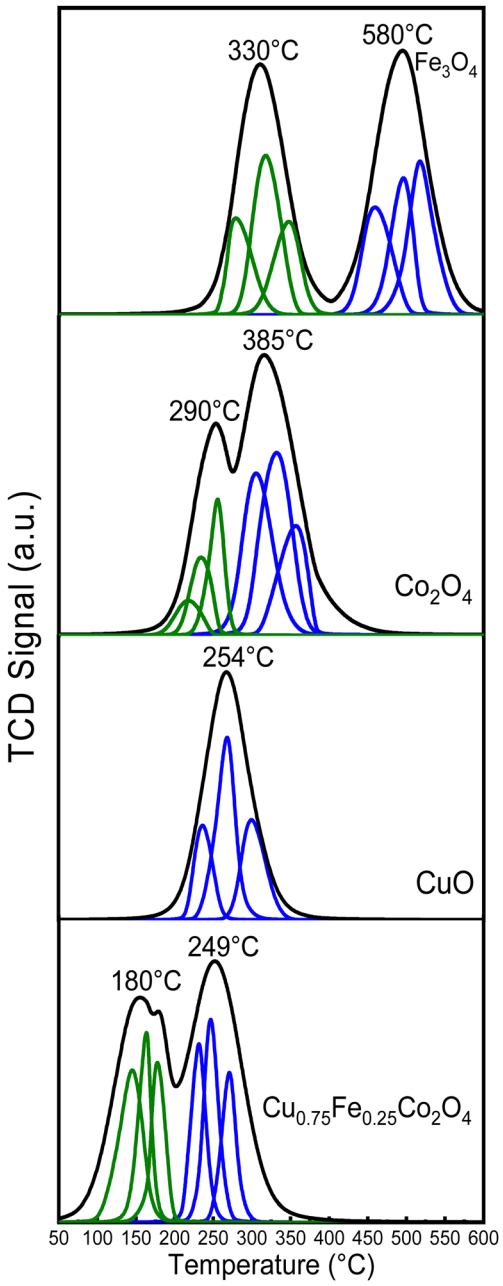

Fig. 7 H_2-TPR profiles of spinel CuO, Co_3O_4, Fe_3O_4 and $Cu_{0.75}Fe_{0.25}Co_2O_4$.

improved the extraction of $O_{Lat.}$ species and weakened the $Cu_{0.75}Fe_{0.25}Co_2O_4$ bond. It can be thus proposed that the relocation of $O_{Lat.}$ from the bulk to the surface of the $Cu_{0.75}Fe_{0.25}Co_2O_4$ catalyst occurred at a relatively low reduction temperature on account of its easy reduction ability, that is favorable for the improvement of the catalytic performance compared to that of individual single oxide.[10,58]

3. Catalytic performance analysis

To assess the catalytic efficiency of each synthesized sample, C_7H_8 oxidation was measured in the temperature range of 100–300 °C, and the result is displayed in Fig. 8. With regard to all samples shown in Fig. 8, the C_7H_8 conversion is temperature-dependent and increases as the reaction temperature rises. Under 120 °C, there is no readily apparent variation in the performances of the catalysts. However, there is a significant variation in the temperature at which the final total oxidation is achieved. Then, C_7H_8 was gradually, easily and rapidly degraded as the reaction temperature was increased and the following performance order was obtained: $Cu_{0.75}Fe_{0.25}Co_2O_4$ > CuO > Co_3O_4 > Fe_3O_4. When compared to single-metal oxides (CuO, Co_3O_4, and Fe_3O_4), the spinel $Cu_{0.75}Fe_{0.25}Co_2O_4$ sample exhibits a higher catalytic performance, reaching 50, 90, and 100% conversion into CO_2 and H_2O at 190, 210, and 220 °C, respectively. Co_3O_4 and Fe_3O_4 exhibit the least effective performance of the tested catalysts, with only a 20% conversion at around 205 °C. Furthermore, the performance of a single CuO at T_{100} = 230 °C is of about 10 °C, which is slightly lower than that of $Cu_{0.75}Fe_{0.25}Co_2O_4$ (T_{100} = 220 °C), while there is a significant shift in T_{50} in the direction of the low reaction temperature compared to Co_3O_4 and Fe_3O_4. It is clear from the catalytic activity tests that the $Cu_{0.75}Fe_{0.25}Co_2O_4$ sample performs better in the deep oxidation of C_7H_8 due to the substitution of Co by Cu and Fe species in the matrix of Co_3O_4, which is responsible for the cooling of the reaction temperatures. The results clearly indicated that the performance of the $Cu_{0.75}Fe_{0.25}Co_2O_4$ catalyst can be significantly and remarkably improved by the co-presence of Cu and Fe species.

Table 3 The quantitative results of H_2-TPR for Co_3O_4 and $Cu_{0.75}Fe_{0.25}Co_2O_4$ catalysts (see complete results in Table SXX, ESI)

Catalysts	Deconvoluted peaks			Peak area ratio II/I
	Peak no.	Center (°C)	Area	
Co_3O_4	I	278.4	1.01	3.15
		259.2	1.05	
		250.3	1.15	
	II	378.1	3.87	
		352.3	4.10	
		325.7	2.17	
$Cu_{0.75}Fe_{0.25}Co_2O_4$	I	171.9	2.20	1.70
		162.8	2.31	
		149.9	2.10	
	II	271.3	3.7	
		245.4	3.95	
		231.1	3.5	

The active samples (CuO, Co_3O_4, Fe_3O_4, and $Cu_{0.75}Fe_{0.25}Co_2O_4$) in this study were compared with other catalysts from earlier published works in order to more accurately assess their performances. The results are shown in Table 4. According to an analysis of the data in this table, under what at first glance appear to be the same test conditions, CuO, Co_3O_4, Fe_3O_4, and $Cu_{0.75}Fe_{0.25}Co_2O_4$ all demonstrate significantly outstanding catalytic performance.

Two distinct reaction mechanisms involved in the oxidation of C_7H_8 over spinel-type mixed oxides were studied and reported by Hertl and Farrauto.[14,79] Generally, the decomposition of the carbonyl group at the surface of the catalyst is beneficial for the total oxidation of C_7H_8 at a temperature

 © 2023 The Author(s). Published by the Royal Society of Chemistry

Open Access Article. Published on 18 April 2023. Downloaded on 12/4/2025 3:24:02 PM.
This article is licensed under a Creative Commons Attribution 3.0 Unported Licence.

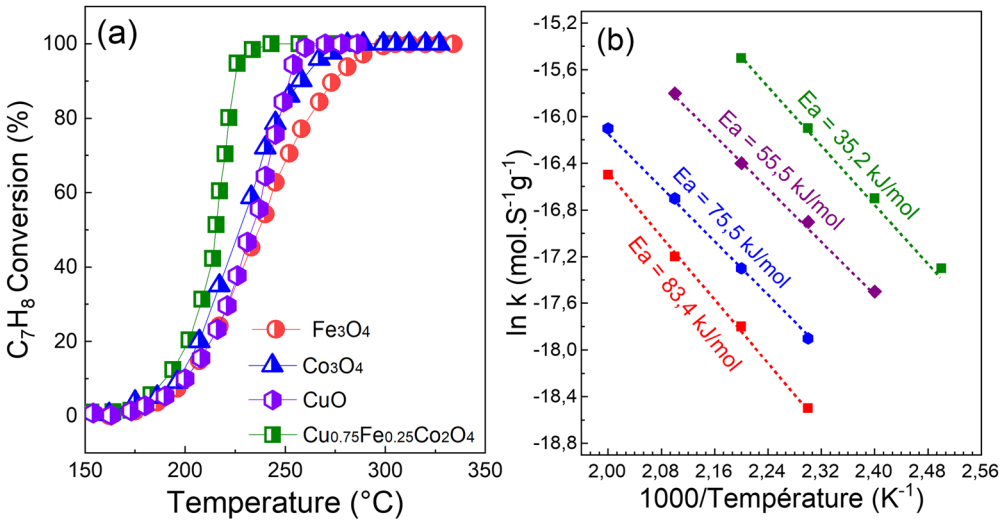

Fig. 8 (a) Light-off curves and (b) apparent activation energy (E_g) of C_7H_8 reaction rates over spinel CuO, Co_3O_4, Fe_3O_4, and $Cu_{0.75}Fe_{0.25}Co_2O_4$.

Table 4 Comparison of the co-precipitation-produced TMOs (CuO, Co_3O_4, Fe_3O_4, and $Cu_{0.75}Fe_{0.25}Co_2O_4$) catalytic efficiency ($T_{50}$, T_{90}) to that of the chosen catalysts from the literature

Material	Weight (mg)	Gas composition	WHSV (mL g^{-1} h^{-1})	T_{50} (°C)	T_{90} (°C)	Ref.
Singles oxides						
CuO	60	5% C_7H_8/20% O_2 in Ar	20 000	237	271	TW
Co_3O_4	60	5% C_7H_8/20% O_2 in Ar	20 000	215	224	TW
Fe_3O_4	60	5% C_7H_8/20% O_2 in Ar	20 000	216	230	TW
CuO	300	1% C_7H_8/21% O_2 in N_2	36 000	370	—	58
MnO_2	100	5% C_7H_8/20% O_2 in Ar	20 000	240	280	59
Co_3O_4	0.06	500 ppm C_7H_8/20% O_2 in Ar	20 000	289	292	10
Mn_2O_3	100	1000 ppm C_7H_8/20% O_2 in Ar	60 000	241	275	60
Fe_2O_3	600	500 ppm C_7H_8/10% O_2 in N_2	50 000	312	338	61
Co_3O_4 nanoclusters	300	1000 ppm C_7H_8/10% O_2 in N_2	20 000	264	277	62
CeO_2/SBA-15	60	0.2% C_7H_8/4.6% O_2 in He	36 000	319	410	63
Co_3O_4	50	2.5 C_7H_8/5% O_2 H_2O	36 000	275	300	64
MnOx	100	100 ppm C_7H_8/2.5% H_2O	20 000	240	290	65
3D Co_3O_4 nanoflower	0.1	1000 ppm C_7H_8/20% O_2 in N_2	48 000	229	274	66
Mixed oxides						
$Cu_{0.75}Fe_{0.25}Co_2O_4$	60	5% C_7H_8/20% O_2 in Ar	20 000	189	215	TW
$Co_{2.3}Zr_{0.27}O_4$	50	2.5 C_7H_8/5% O_2 H_2O	36 000	250	270	64
$Mn_xCo_yCe_zO_n$	5	1000 ppm C_7H_8/20% O_2 in N_2	100 000	216	249	67
LaFeO	200	1% C_7H_8/20% O_2 in N_2	100 000	260	282	68
Co_2AlO_4	3482	1% C_7H_8/20% O_2 in N_2	100 000	300	325	62
$MgCo_2O_4$	100	2.5 C_7H_8/5% O_2 H_2O	36 000	242	250	10
Co–Zr	600	2.5 C_7H_8/5% O_2 H_2O	36 000	251	278	41
MnOx–CeO_2	300	1000 ppm C_7H_8/20% O_2 in N_2	60 000	212	220	69
$Cu_{0.8}Mn_2Ce_{0.2}Ox$	200	2000 ppm C_7H_8, air balance	10000	240	275	70
Cu_2Mn_1O		1000 ppm C_7H_8/20% O_2 in N_2	60 000	224	229	71
$CuCe_{0.75}Zr_{0.25}/TiO_2$	300	0.5% C_7H_8, air balance	60 000	225	234	72
Supported noble metals						
Ag/MnO_2	60	500 ppm C_7H_8/10% O_2 in N_2	36 000	200	210	59
Pt-MOR	300	1000 ppm C_7H_8/20% O_2 in N_2	60 000	190	220	73
Pt–pdAl_2O_3	600	950 ppm C_7H_8/20% O_2 in N_2	19 500	188	214	74
Pt–pd-HMS	200	1000 ppm C_7H_8/20% O_2 in N_2	26 000	200	235	75
Ag–CeO_2/SBA-15	100	0.2% C_7H_8/4.6% O_2 in He	36 000	234	250	63
Ag_2O/SBA-15	300	0.2% C_7H_8/4.6% O_2 in He	100 000	255	270	63
Pd/SiO_2	60	1% C_7H_8/20% O_2 in N_2	100 000	185	218	76
Pd/NiO	0.5	500 ppm C_7H_8/10% O_2 in N_2	180 000	200	230	77
Pt/Al_2O_3(S)–I	100	1% C_7H_8/20% O_2 in N_2	24 000	240	265	78
Pt–Pd–Al_2O_3	600	1% C_7H_8/20% O_2 in N_2	1950	190	215	74

ranging from 80 to 200 °C. According to Hertl *et al.*, metal oxide surface lattice oxygen generally reacts with C_7H_8 molecules at low temperatures (80–200 °C), while carbonate groups from adsorbed oxygen participate in C_7H_8 total oxidation above

Open Access Article. Published on 18 April 2023. Downloaded on 12/4/2025 3:24:02 PM.
This article is licensed under a Creative Commons Attribution 3.0 Unported Licence.

~200 °C and form H_2O and CO_2.[79] Moreover, it is also possible that an Eley–Rideal (ER) mechanism can be used to complete the oxidation of C_7H_8 over $Cu_{0.75}Fe_{0.25}Co_2O_4$ nanoparticles, with an excessive amount of absorbed oxygen species, serving as active oxygen species. This result shows that co-doping of Co_3O_4 with Cu and Fe had a significant impact on the physicochemical characteristics of $Cu_{0.75}Fe_{0.25}Co_2O_4$. This is because the co-doping provides excellent thermal conductivity and scattering of the charge carrier *via* agglomeration of copper, iron, and cobalt, leading to better catalytic performance than that of single-metal oxides.[80]

It has been well established that Polaron jumps can cause an increase in the electrical conductivity of the spinel oxide between the nearby octahedron cations.[81] As a result, anionic vacancies near octahedral cations may be suitable location to trap oxygen species. This can increase the electrical resistivity by increasing the distance between octahedral site anions and also improve the catalytic performance by allowing for mass transfer of reactive oxygen species. Numerous characteristics including crystal size and structure, morphology, chemical composition, surface metal content, and oxygen species of a metal oxide catalyst have been reported to have a significant impact on the low-temperature C_7H_8 catalytic oxidation.[15] Therefore, the fast mobility of reactive oxygen species, high active surface area, and good porosity, which result in a long contact time between catalysts and reactants provided by the ternary oxide, as well as the synergetic effects of (Cu, Fe, and Co) metal species, could also be beneficial for the catalytic performance. When ternary oxide ($Cu_{0.75}Fe_{0.25}Co_2O_4$) NCs are used as catalysts for C_7H_8 oxidation, the additional role of synergistic effects among Cu^{2+}, Fe^{3+}, and Co^{3+} is to enhance the catalytic activity. Additionally, the microstructure analysis revealed a dome top-like morphology with exposition of active sites, which could absorb more oxygen and expose more surface area, leading to the oxidation at relatively low temperatures. In addition, the apparent activation energies (E_{appa}), calculated using the Arrhenius equation based on the light-off curve in the region where the C_7H_8 conversion was less than 15%,[22] were used to compare the catalytic activity.[22] Fig. 8b shows the comparison between the achieved E_{appa} in the current work and the apparent activation energies reported in the literature. Compared to the corresponding E_{appa} values of pure copper oxide (55.5 kJ mol^{-1}), cobalt oxide (75.5 kJ mol^{-1}), and iron oxide (83.4 kJ mol^{-1}) in the C_7H_8 total oxidation reaction, E_{appa} of $Cu_{0.75}Fe_{0.25}Co_2O_4$ was found to be the smallest (35.2 kJ mol^{-1}). The E_{appa} of ternary $Cu_{0.75}Fe_{0.25}Co_2O_4$ in its as-prepared state shows that, the agglomeration of the corresponding oxide leads to a dramatic decrease in the E_{appa}, while the E_g^{Opt} is becoming narrow with the decrease of the particle size (see Fig. 9) which in turn promotes the catalytic performance as mentioned previously.[11]

3.1. Reaction mechanism study

In order to explore and propose a possible reaction mechanism involved in the toluene total oxidation over $Cu_{0.75}Fe_{0.25}Co_2O_4$, *in situ* DRIFTS experiments were performed. The experiment was performed at several temperatures and for each temperature, the reaction was maintained for 2 hours. Fig. 10 displays the typical *in situ* DRIFTS spectra at a reaction temperature ranging from 100 to 230 °C. The typical adsorption bands of toluene can be divided into three wavenumber regions ranging from 1560 to 1355; 1850 to 1610 and 2360 to 2338 cm^{-1}, which can be attributed to the acid carboxylic group, the stretching

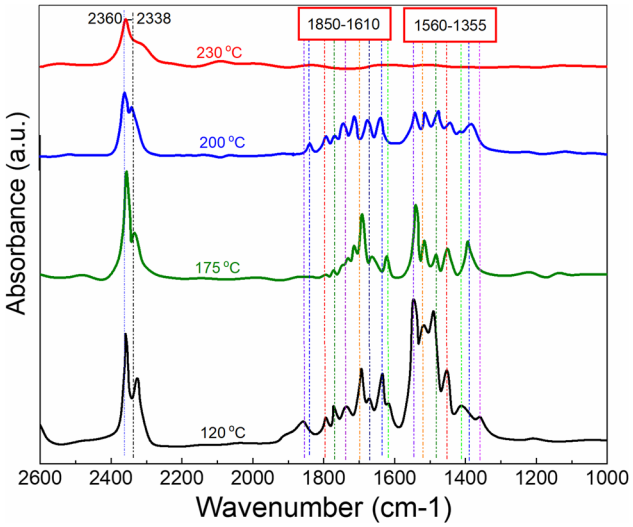

Fig. 10 *In situ* DRIFTS spectra of toluene total oxidation as a function of temperature over $Cu_{0.75}Fe_{0.25}Co_2O_4$ in a feed gas composed of 500 ppm toluene + O_2 dilute in Ar.

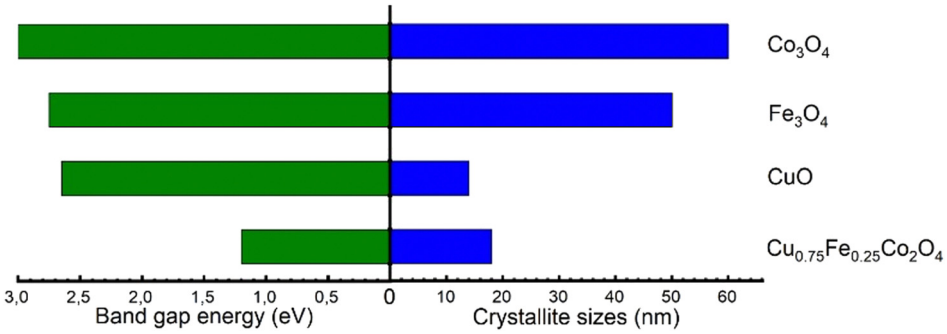

Fig. 9 Variation in the optical band gap energy (E_g) *vs.* particle size for the overall samples.

 © 2023 The Author(s). Published by the Royal Society of Chemistry

Open Access Article. Published on 18 April 2023. Downloaded on 12/4/2025 3:24:02 PM.
This article is licensed under a Creative Commons Attribution 3.0 Unported Licence.

vibration mode of C═O and adsorbed and/or gaseous carbon monoxide respectively. The asymmetric υ(C═O) stretching vibration signals detected around 1560 cm^{-1} indicate the occurrence of intermediate products during the reaction process[18,82] while the most intense band assigned to carboxylate species (1355–1560 cm^{-1}) makes us believe that benzoate is the crucial intermediate. The signal located at the neighbourhood of 1355 cm^{-1} is ascribed to the acetate species in agreement with the literature.[19] The typical signal of toluene initially increased and later decreased as the temperature increased from 120 to 200 °C, attesting that toluene was effectively decomposed to maleic anhydride species and gradually agglomerated onto the surface of $Cu_{0.75}Fe_{0.25}Co_2O_4$. Upon further increase in the reaction temperature to 230 °C, the corresponding benzoate signals (1560–1355 cm^{-1}) totally vanish. This may be due to the further conversion of intermediates (benzyl alcohol/benzoate) to anhydride/acetate, followed by oxidation and complete transformation into CO_2 and H_2O. Based on the *in situ* DRIFTS analysis, a most plausible mechanism of toluene total oxidation is proposed as follows: toluene was first adsorbed at the active sites, transformed to a benzyl derivative followed by anhydride and acetate formation, before complete conversion into CO_2 and H_2O, as displayed in Fig. 11. In this process, indeterminate species vacate from the surface of $Cu_{0.75}Fe_{0.25}Co_2O_4$ to create O_v; afterwards, the catalyst upholds gaseous oxygen in the airflow to replenish O_v. Herein, it is worth nothing that the rate-determining step in the toluene deep oxidation is the breakage of the aromatic ring.

3.2. Stability and reproducibility test of $Cu_{0.75}Fe_{0.25}Co_2O_4$

The catalyst durability test also known as stability under prolonged time-on-stream (TOS) was performed at a constant reaction temperature (T_{100} = ∼225 °C). This experiment was performed in order to evaluate the catalyst ability to remain stable under prolonged reactions. The catalyst ability to reproduce results and the long-term stability are some of the key criteria required for their industrial applications. Herein, both experimental tests were performed, and the results are presented in Fig. 12.

The cycling stability of the $Cu_{0.75}Fe_{0.25}Co_2O_4$ catalyst was performed, and the results are presented in Fig. 12a. The results show that the $Cu_{0.75}Fe_{0.25}Co_2O_4$ catalyst exhibits excellent cycling stability, after 3 consecutive running steps, indicating a good potential for industrial application as revealed by the excellent cycling stability results. Additionally, stability tests for the $Cu_{0.75}Fe_{0.25}Co_2O_4$ sample have been performed over 800 min at a constant T_{100} = 225 °C, as shown in Fig. 12b. The results indicated that $Cu_{0.75}Fe_{0.25}Co_2O_4$ catalysts revealed excellent durability upon continuous toluene conversion, and no significant deactivation was noticed after 800 min time-on-stream. From the obtained results, $Cu_{0.75}Fe_{0.25}Co_2O_4$ maintained over 96% toluene conversion and just a negligible decrement in performances of 4% was observed and can be assigned to the coverage of the surface-active sites on $Cu_{0.75}Fe_{0.25}Co_2O_4$ NCs by soot particles generated during the oxidation process.

4. Experimental

4.1. Catalyst preparation

The NCs of CuO, Fe_3O_4, Co_3O_4 and $Cu_{0.75}Fe_{0.25}Co_2O_4$ were prepared by a co-precipitation method and the experimental procedure is detailed below.

4.1.1. Synthesis of single oxides (CuO, Fe_3O_4, Co_3O_4). First, 0.03 mol of hydrate copper sulfate ($CuSO_4{\cdot}5H_2O$), hydrate iron sulfate ($FeSO_4{\cdot}5H_2O$) and cobalt acetylacetonate ($Co(acac)_3$) were mixed solely to 10 mL of ethanol and the obtained mixture was kept at 80 °C under continuous magnetic stirring, after which a solution of oxalic acid (0.25 mol L^{-1}) was rapidly added. The obtained solution was then cooled to ∼60 °C, and after 30 minutes, a precipitate was obtained that was directly centrifuged and washed several times with deionized water and twice with ethanol. The resulting precipitate was

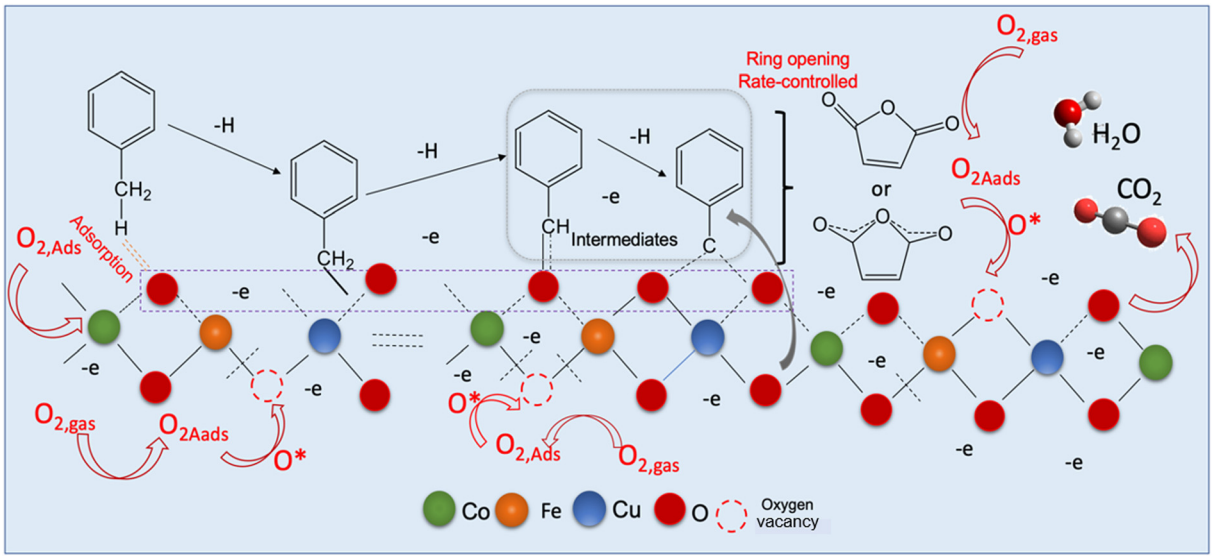

Fig. 11 Proposed reaction mechanism of toluene oxidation over the $Cu_{0.75}Fe_{0.25}Co_2O_4$ catalyst.

Open Access Article. Published on 18 April 2023. Downloaded on 12/4/2025 3:24:02 PM.
This article is licensed under a Creative Commons Attribution 3.0 Unported Licence.

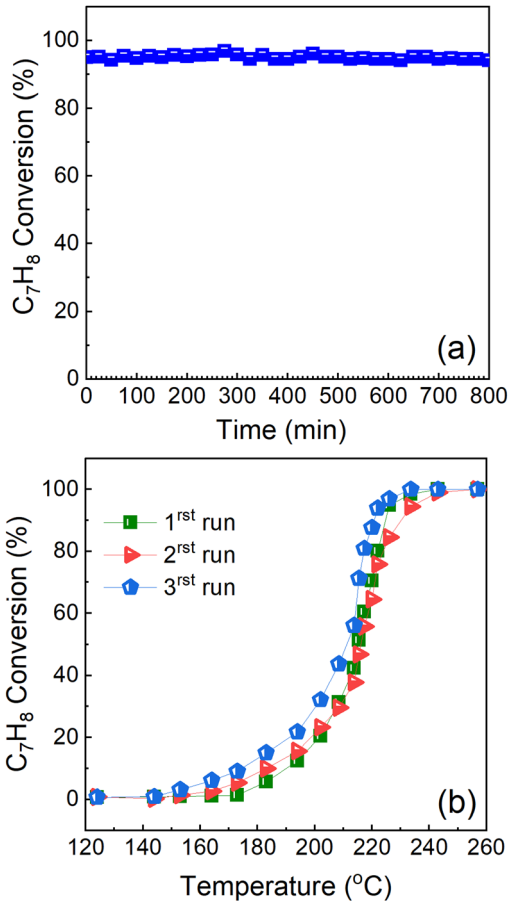

Fig. 12 (a) Reproducibility/stability and (b) long-term durability test study of $Cu_{0.75}Fe_{0.25}Co_2O_4$ in DME deep oxidation with time-on-stream at 225 °C.

dried in an oven at 105 °C for 24 h and finally annealed at 400 °C in air for 3 h.

4.1.2. Synthesis of ternary oxide (CuFeCoO). First, $CuSO_4 \cdot 5H_2O$, $FeSO_4 \cdot 5H_2O$ and $Co(acac)_3$ precursors at appropriate ratios of Cu/Fe/Co = 0.75/0.25/2 were mixed together with 40 mL of ethanol. The obtained mixture was then subjected to all the above-mentioned steps for single oxide synthesis.

4.2. Catalyst characterization

Numerous analysis tools were used to analyze the thermally treated CuO, Fe_3O_4, Co_3O_4 and CuFeCoO NPs. The details of the characterization methods are presented in ESI 1.†

4.3. Catalytic activity analysis

The catalytic behavior of CuO, Fe_3O_4, Co_3O_4 and $Cu_{0.75}Fe_{0.25}Co_2O_4$ was investigated using a tubular fixed-bed reactor system, and 0.6 g of catalyst was placed in a fixed-bed rector. Complete details of the catalytic performance tests are given in ESI 2.†

5 Conclusions

In conclusion, single-oxide (CuO, Co_3O_4, Fe_3O_4) and ternary mixed-oxide ($Cu_{0.75}Fe_{0.25}Co_2O_4$) catalysts for C_7H_8 oxidation have been successfully synthesized *via* a simple co-precipitation approach. Analyses were performed on the catalyst's structure, morphology, composition, and ionic states as well as its optical energy band gap properties. In addition, H_2-TPR was used to analyze the reduction characteristics of the prepared oxides. XRD and FTIR analysis revealed nano-sized crystallites. The results of the SEM analysis of the surface microstructure revealed a dome top-like morphology for ternary $Cu_{0.75}Fe_{0.25}Co_2O_4$, a homogeneous morphology with fine interconnected particles for CuO, a densely packed morphology for Fe_3O_4 and a cubic morphology for Co_3O_4. Ternary $Cu_{0.75}Fe_{0.25}Co_2O_4$ exhibits the lowest bandgap energy and reducing properties compared to the synthesized single-metal oxides. The catalytic tests indicated that ternary $Cu_{0.75}Fe_{0.25}Co_2O_4$ was the most active sample compared with the single oxides CuO, Co_3O_4, and Fe_3O_4. The attractive catalytic performance of ternary $Cu_{0.75}Fe_{0.25}Co_2O_4$ was assigned to the combination of synergistic effects between cation sites (Cu^{2+}, Fe^{2+}, Fe^{3+}, Co^{2+}, and Co^{3+}) and chemisorbed oxygen species (O_2^{2-}, and O^-), low-temperature reducibility, low E_g^{opt}, the open porosity observed on the morphology as well as the greater number of oxygen species that provided ideal active sites for the oxidation reaction. Due to the high efficiency, ecological friendliness, and energy-saving qualities of the co-precipitation technique, this work offered a novel method for the development of effective ternary oxides. Therefore, co-doping of Cu and Fe to obtain trimetallic oxides with spinel structure is an effective and useful strategy to enhance the catalytic behavior of single Co_3O_4 with spinel structure.

Author contributions

Hippolyte Todou Assaouka: conceptualization, data curation, formal analysis, investigation, validation, methodology, visualization, writing – original draft. Issah Ngouh Nsangou: conceptualization, data curation, formal analysis, investigation, validation, methodology, visualization, writing – original draft, Daniel Manhouli Daawe: methodology, data curation, formal analysis, visualization, software. Daniel Onana Mevoa: formal analysis, methodology. Abraham Atour Zigla: resources, methodology, writing – review & editing. Patrick Ndouka Ndouka: methodology, data curation, formal analysis, visualization. Patrick Mountapmbeme Kouotou: conceptualization, visualization, formal analysis, writing – original draft, writing – review & editing, funding acquisition, supervision.

Conflicts of interest

There are no conflicts to declare.

Acknowledgements

Dr Muhammad Waqas from the Department of Mechanical Engineering, College of Engineering and Technology, University of Sargodha, Sargodha 40100, Pakistan is deeply acknowledged to have facilitated some analysis in the present study.

 © 2023 The Author(s). Published by the Royal Society of Chemistry

Open Access Article. Published on 18 April 2023. Downloaded on 12/4/2025 3:24:02 PM.
This article is licensed under a Creative Commons Attribution 3.0 Unported Licence.

References

1 N. Li and F. Gaillard, *Appl. Catal., B*, 2009, **88**, 152–159.
2 F. N. Aguero, B. P. Barbero, L. Gambaro and L. E. Cadús, *Appl. Catal., B*, 2009, **91**, 108–112.
3 K. F. Kalz, R. Kraehnert, M. Dvoyashkin, R. Dittmeyer, R. Gläser, U. Krewer, K. Reuter and J.-D. Grunwaldt, *ChemCatChem*, 2017, **9**, 17–29.
4 A. Sharma and B.-K. Lee, *Appl. Catal., A*, 2016, **523**, 272–282.
5 X. Wang, K. Huang, J. Qian, Y. Cong, C. Ge and S. Feng, *Sci. Bull.*, 2017, **62**, 658–664.
6 W. Tang, W. Xiao, S. Wang, Z. Ren, J. Ding and P.-X. Gao, *Appl. Catal., B*, 2018, **226**, 585–595.
7 M. Wang, D. Chen, N. Li, Q. Xu, H. Li, J. He and J. Lu, *ACS Appl. Mater. Interfaces*, 2020, **12**, 13781–13789.
8 Q. Zhang, S. Mo, J. Li, Y. Sun, M. Zhang, P. Chen, M. Fu, J. Wu, L. Chen and D. Ye, *Catal. Sci. Technol.*, 2019, **9**, 4538–4551.
9 L. Li, F. Zhang, Z. Zhong, M. Zhu, C. Jiang, J. Hu and W. Xing, *Ind. Eng. Chem. Res.*, 2017, **56**, 13857–13865.
10 A. A. Zigla, T. Kox, D. Mevoa, H. T. Assaouka, I. N. Nsangou, D. M. Daawe, S. Kenmoe and P. M. Kouotou, *Catalysts*, 2022, **12**, 411.
11 P. M. Kouotou, H. Vieker, Z. Y. Tian, P. T. Ngamou, A. El Kasmi, A. Beyer, A. Gölzhäuser and K. Kohse-Höinghaus, *Catal. Sci. Technol.*, 2014, **4**, 3359–3367.
12 Y. Dong, J. Zhao, J.-Y. Zhang, Y. Chen, X. Yang, W. Song, L. Wei and W. Li, *Chem. Eng. J.*, 2020, **388**, 124244.
13 R. Huang, L. Luo, W. Hu, Z. Tang, X. Ji, L. Chen, Z. Yu, Y. Zhang, D. Zhang and P. Xiao, *Catal. Sci. Technol.*, 2022, **12**, 4157–4168.
14 P. M. Kouotou, M. Waqas, A. El Kasmi, Z. Atour and Z.-Y. Tian, *Appl. Catal., A*, 2021, **612**, 117990.
15 S.-B. Fan, P. M. Kouotou, J.-J. Weng, G.-F. Pan and Z.-Y. Tian, *Proc. Combust. Inst.*, 2017, **36**, 4375–4382.
16 L. F. Liotta, *Appl. Catal., B*, 2010, **100**, 403–412.
17 V. H. Vu, J. Belkouch, A. Ould-Dris and B. Taouk, *AIChE J.*, 2008, **54**, 1585–1591.
18 S. Mo, Q. Zhang, J. Li, Y. Sun, Q. Ren, S. Zou, Q. Zhang, J. Lu, M. Fu and D. Mo, *Appl. Catal., B*, 2020, **264**, 118464.
19 C. Dong, Z. Qu, Y. Qin, Q. Fu, H. Sun and X. Duan, *ACS Catal.*, 2019, **9**, 6698–6710.
20 G. Li, C. Zhang, Z. Wang, H. Huang, H. Peng and X. Li, *Appl. Catal., A*, 2018, **550**, 67–76.
21 Q. Ren, S. Mo, R. Peng, Z. Feng, M. Zhang, L. Chen, M. Fu, J. Wu and D. Ye, *J. Mater. Chem. A*, 2018, **6**, 498–509.
22 Z.-Y. Tian, P. H. T. Ngamou, V. Vannier, K. Kohse-Höinghaus and N. Bahlawane, *Appl. Catal., B*, 2012, **117**, 125–134.
23 Q. Fu, H. Saltsburg and M. Flytzani-Stephanopoulos, *Science*, 2003, **301**, 935–938.
24 S. D. Park, S. Won Lee, S. Kang, I. C. Bang, J. H. Kim, H. S. Shin, D. W. Lee and D. Won Lee, *Appl. Phys. Lett.*, 2010, **97**, 023103.
25 J. A. Rodriguez, *Catal. Today*, 2003, **85**, 177–192.
26 H. Jiang, X. Xu, R. Zhang, Y. Zhang, J. Chen and F. Yang, *RSC Adv.*, 2020, **10**, 5116–5128.
27 S. Khan and A. K. Narula, *Mater. Sci. Eng., B*, 2019, **243**, 86–95.
28 X. Cao, E. Johnson and M. Nath, *ACS Sustainable Chem. Eng.*, 2019, **7**, 9588–9600.
29 M. Waqas, P. M. Kouotou, A. El Kasmi, Y. Wang and Z.-Y. Tian, *Chin. Chem. Lett.*, 2020, **31**, 1201–1206.
30 N. V. Suramwar, S. R. Thakare and N. T. Khaty, *Int. J. Nano Dimens.*, 2012, **3**, 75–80.
31 D. Lu, O. A. Zelekew, A. K. Abay, Q. Huang, X. Chen and Y. Zheng, *RSC Adv.*, 2019, **9**, 2018–2025.
32 K. Qadir, S. H. Joo, B. S. Mun, D. R. Butcher, J. R. Renzas, F. Aksoy, Z. Liu, G. A. Somorjai and J. Y. Park, *Nano Lett.*, 2012, **12**, 5761–5768.
33 J. Ma, J. Teo, L. Mei, Z. Zhong, Q. Li, T. Wang, X. Duan, J. Lian and W. Zheng, *J. Mater. Chem.*, 2012, **22**, 11694–11700.
34 R. Lakshmi and S. Sasikumar, *Int. J. Nanomed.*, 2015, **10**, 129.
35 N. Bahlawane, E. F. Rivera, K. Kohse-Höinghaus, A. Brechling and U. Kleineberg, *Appl. Catal., B*, 2004, **53**, 245–255.
36 T. Yamashita and P. Hayes, *Appl. Surf. Sci.*, 2008, **254**, 2441–2449.
37 J. Cheng, J. Yu, X. Wang, L. Li, J. Li and Z. Hao, *Energy Fuels*, 2008, **22**, 2131–2137.
38 F. Bao, X. Wang, X. Zhao, Y. Wang, Y. Ji, H. Zhang and X. Liu, *Catal. Sci. Technol.*, 2014, **13**, 22–25.
39 H. Gao, X. Wang, G. Wang, C. Hao, C. Huang and C. Jiang, *J. Mater. Chem. C*, 2019, **7**, 13267–13278.
40 M. A. Zamudio, S. Bensaid, D. Fino and N. Russo, *Ind. Eng. Chem. Res.*, 2011, **50**, 2622–2627.
41 X. Zhang, M. Zhao, Z. Song, H. Zhao, W. Liu, J. Zhao and Y. Xing, *New J. Chem.*, 2019, **43**, 10868–10877.
42 W. Liu, B. Wang, C. Cui, Y. Zhang, L. Wang and Z. Wang, *Mater. Lett.*, 2021, **289**, 129378.
43 C. Chen, L. Liu, Y. Li, W. Li, L. Zhou, Y. Lan and Y. Li, *Chem. Eng. J.*, 2020, **384**, 123257.
44 C. Song, Z. Zhao, H. Li, D. Wang and Y. Yang, *RSC Adv.*, 2016, **6**, 102931–102937.
45 T. Yanom, M. Ebizuka, S. Shibata and M. Yamane, *J. Electron Spectrosc. Relat. Phenom.*, 2003, **131–132**, 133–144.
46 J. Lei, S. Wang and J. Li, *Ind. Eng. Chem. Res.*, 2020, **59**, 5583–5590.
47 K. Wang, Y. Cao, J. Hu, Y. Li, J. Xie and D. Jia, *ACS Appl. Mater. Interfaces*, 2017, **9**, 16128–16137.
48 P. Li, D. E. Miser, S. Rabiei, R. T. Yadav and M. R. Hajaligol, *Appl. Catal., B*, 2003, **43**, 151–162.
49 L. F. Liotta, H. Wu, G. Pantaleo and A. M. Venezia, *Catal. Sci. Technol.*, 2013, **3**, 3085–3102.
50 S. Sheik Fareed, N. Mythili, H. Mohamed Mohaideen, K. Saravanakumar, R. Chandramohan and G. Ravi, *J. Mater. Sci.: Mater. Electron.*, 2016, **27**, 3420–3426.
51 A. A. Ansari, J. P. Labis, M. Alam, S. M. Ramay, N. Ahmad and A. Mahmood, *Acta Metall. Sin. (Engl. Lett.)*, 2016, **29**, 265–273.
52 E. Lee, A. Benayad, T. Shin, H. Lee, D.-S. Ko, T. S. Kim, K. S. Son, M. Ryu, S. Jeon and G.-S. Park, *Sci. Rep.*, 2014, **4**, 1–8.
53 A. N. Banerjee and K. K. Chattopadhyay, *Prog. Cryst. Growth Charact. Mater.*, 2005, **50**, 52–105.

Open Access Article. Published on 18 April 2023. Downloaded on 12/4/2025 3:24:02 PM.
This article is licensed under a Creative Commons Attribution 3.0 Unported Licence.

54 A. K. M. Alsmadi, B. Salameh and M. Shatnawi, *J. Phys. Chem. C*, 2020, **124**, 16116–16126.
55 Z.-Y. Tian, N. Bahlawane, V. Vannier and K. Kohse-Höinghaus, *Proc. Combust. Inst.*, 2013, **34**, 2261–2268.
56 Y.-H. Lin, H. Faber, J. G. Labram, E. Stratakis, L. Sygellou, E. Kymakis, N. A. Hastas, R. Li, K. Zhao and A. Amassian, *Adv. Sci.*, 2015, **2**, 1500058.
57 S. Zhang, J. Ma, Z. Hu, G. Cui and L. Chen, *Chem. Mater.*, 2019, **31**, 6033–6065.
58 C. He, Y. Yu, L. Yue, N. Qiao, J. Li, Q. Shen, W. Yu, J. Chen and Z. Hao, *Appl. Catal., B*, 2014, **147**, 156–166.
59 Y. Qin, Y. Wang, J. Li and Z. Qu, *Surf. Interfaces*, 2020, **21**, 100657.
60 X. Yang, X. Yu, M. Lin, X. Ma and M. Ge, *Catal. Today*, 2019, **327**, 254–261.
61 Y. Wang, L. Zhang and L. Guo, *ACS Appl. Nano Mater.*, 2018, **1**, 1066–1075.
62 Q. Zhang, S. Mo, B. Chen, W. Zhang, C. Huang and D. Ye, *Mol. Catal.*, 2018, **454**, 12–20.
63 N. N. Mikheeva, V. I. Zaikovskii, Y. V. Larichev and G. V. Mamontov, *Mater. Today Chem.*, 2021, **21**, 100530.
64 M. Wang, D. Chen, N. Li, Q. Xu, H. Li, J. He and J. Lu, *Small*, 2020, **16**, 2005715.
65 M. Li, C. Zhang, L. Fan, Y. Lian, X. Niu and Y. Zhu, *ACS Appl. Mater. Interfaces*, 2021, **13**, 10089–10100.
66 Q. Ren, Z. Feng, S. Mo, C. Huang, S. Li, W. Zhang, L. Chen, M. Fu, J. Wu and D. Ye, *Catal. Today*, 2019, **332**, 160–167.
67 H. Chen, W. Cui, D. Li, Q. Tian, J. He, Q. Liu, X. Chen, M. Cui, X. Qiao and Z. Zhang, *Ind. Eng. Chem. Res.*, 2020, **59**, 10804–10812.
68 J. Yang, S. Liu, T. He, L. C. Nengzi, Y. Wang, L. Su and M. Geng, *J. Environ. Chem. Eng.*, 2021, **9**, 106361.
69 H. Sun, X. Yu, X. Ma, X. Yang, M. Lin and M. Ge, *Catal. Today*, 2020, **355**, 580–586.
70 B. Heidinger, S. Royer, J.-M. Giraudon, O. Gardoll, H. Alamdari and J.-F. Lamonier, *ChemCatChem*, 2020, **12**, 2271–2282.
71 J. Hu, W. B. Li and R. F. Liu, *Catal. Today*, 2018, **314**, 147–153.
72 C. Zhao, Q. Hao, Q. Zhang, N. Yan, J. Liu, B. Dou and F. Bin, *Appl. Catal., A*, 2019, **569**, 66–74.
73 J. Zhang, C. Rao, H. Peng, C. Peng, L. Zhang, X. Xu, W. Liu, Z. Wang, N. Zhang and X. Wang, *Chem. Eng. J.*, 2018, **334**, 10–18.
74 X. Liu, Q. Zhang, P. Ning, T. Tang, J. Hu and W. Su, *Catal. Commun.*, 2018, **115**, 26–30.
75 Q. Zhang, W. Su, P. Ning, X. Liu, H. Wang and J. Hu, *Chem. Eng. Sci.*, 2019, **205**, 230–237.
76 H. Wang, Y. Zhang, M. Wu, H. Xu, X. Jin, J. Zhou and Z. Hou, *Ind. Eng. Chem. Res.*, 2020, **59**, 20316–20324.
77 Q. Meng, J. Liu, X. Weng, P. Sun, J. A. Darr and Z. Wu, *Catal. Sci. Technol.*, 2018, **8**, 1858–1866.
78 T. Gan, X. Chu, H. Qi, W. Zhang, Y. Zou, W. Yan and G. Liu, *Appl. Catal., B*, 2019, **257**, 117943.
79 W. Hertl and R. J. Farrauto, *J. Catal.*, 1973, **29**, 352–360.
80 G. E. Childs, L. J. Ericks and R. L. Powell, *Mater. Today Chem.*, 2019, **11**, 215–220.
81 E. J. W. Verwey, *Ind. Eng. Chem. Res.*, 1951, **155**, 322–331.
82 M. Li, K. N. Hui, K. S. Hui, S. K. Lee, Y. R. Cho, H. Lee, W. Zhou, S. Cho, C. Y. H. Chao and Y. Li, *Appl. Catal., B*, 2011, **107**, 245–252.

 © 2023 The Author(s). Published by the Royal Society of Chemistry